ACSNANO
www.acsnano.org
ARTICLE

Double Epitaxy as a Paradigm for Templated Growth of Highly Ordered Three-Dimensional Mesophase Crystals

Yongsoon Shin, Jinhui Tao, Bruce W. Arey, Chongmin Wang, Gregory J. Exarhos, James J. De Yoreo, Maria L Sushko,* and Jun Liu*

Pacific Northwest National Laboratory, Richland, Washington 99352, United States

Supporting Information

ABSTRACT: **Molecular templating and self-assembly are fundamental mechanisms for controlling the morphology of biominerals, while in synthetic two-dimensional layered materials similar levels of control over materials structure can be achieved through the epitaxial relationship with the substrate. In this study these two concepts are combined to provide an approach for the nucleation and growth of three-dimensional ordered mesophases on solid surfaces. A combined experimental and theoretical study revealed how atomic ordering of the substrate controls the structure of surfactant template and the orientation and morphology of the epitaxially grown inorganic material. This dual epitaxial relationship between the substrate, surfactant template, and inorganic mesophase gives rise to a highly ordered porous mesophase with a well-defined cubic lattice of pores. The level of control over the material's three-dimensional architecture achieved in this one-step synthesis is reminiscent of that in biomineralization.**

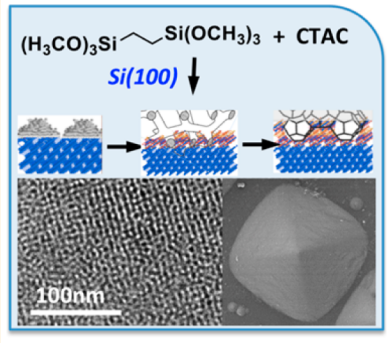

KEYWORDS: *crystal growth, epitaxy, self-assembly, porous materials*

Heterogeneous substrate controlled nucleation is a widespread phenomenon in both the synthesis of materials and natural processes of biomineralization. In synthetic materials such substrate-controlled crystal growth often involves atomic-scale epitaxy between the substrate and the crystal.[1−5] This method is widely used for the growth of atomically controlled thin films,[6−8] However, achieving the same level of control over crystal morphology at the mesoscale remains a challenge despite a significant effort in developing synthesis approaches for achieving extended ordering in mesoporous materials[9−23] and the importance of such three-dimensional ordered materials for many applications including catalysis, separation, sensing, and energy conversion.[24−27] Here we demonstrate that *mesoscale* ordering of an organic−inorganic composite can be epitaxially controlled by the *atomic* ordering of the substrate. Detailed characterization and computer simulations are used to gain insights into the complex molecular processes leading to the formation of these atomically controlled organic−inorganic composite materials. In particular, we report a pathway for the synthesis of highly ordered mesophase crystals and porous materials, which utilizes dual epitaxial relationships with the substrate: (1) substrate-controlled three-dimensional surfactant templating and (2) metal oxide−substrate epitaxy. The method is demonstrated using the example of the epitaxial solution growth of uniform pyramidal silicates with ordered mesopores on Si(100) surfaces.

RESULTS AND DISCUSSION

The silicate films were synthesized using a two-step process (see Methods for more details). First, a BTME (1,2-bis(trimethoxysilyl)ethane)/CTAC (cetyltrimethylammonium chloride)/NaOH/H_2O precursor solution was aged for 24 h at room temperature. Then Si(100) substrates were introduced into the solution, which was then heated to 100 °C and held at that temperature for times ranging from 0.5 to 2 h, with some samples exposed to repeated cycles of incubation in solution. Only a clear solution was used in order to avoid deposition onto the Si surface by silicate particles that had precipitated in the bulk solution.

The substrates were then imaged *ex situ* using scanning electron microscopy (SEM) and atomic force microscopy (AFM) (Figure 1).

The SEM images reveal the presence of coaligned pyramidal-shaped microscopic nanoparticles up to 20 μm in width on the Si(100) surfaces (Figure 1a−c). Figure 1d shows a typical SEM image of a large array of the pyramidal particles grown following repeated processing. The pyramids are uniform in shape, but the sizes vary over the range 3−20 μm. The studies of the same samples using AFM demonstrated that untreated,

Received: June 16, 2016
Accepted: August 30, 2016
Published: August 30, 2016

DOI: 10.1021/acsnano.6b03999
ACS Nano 2016, 10, 8670−8675

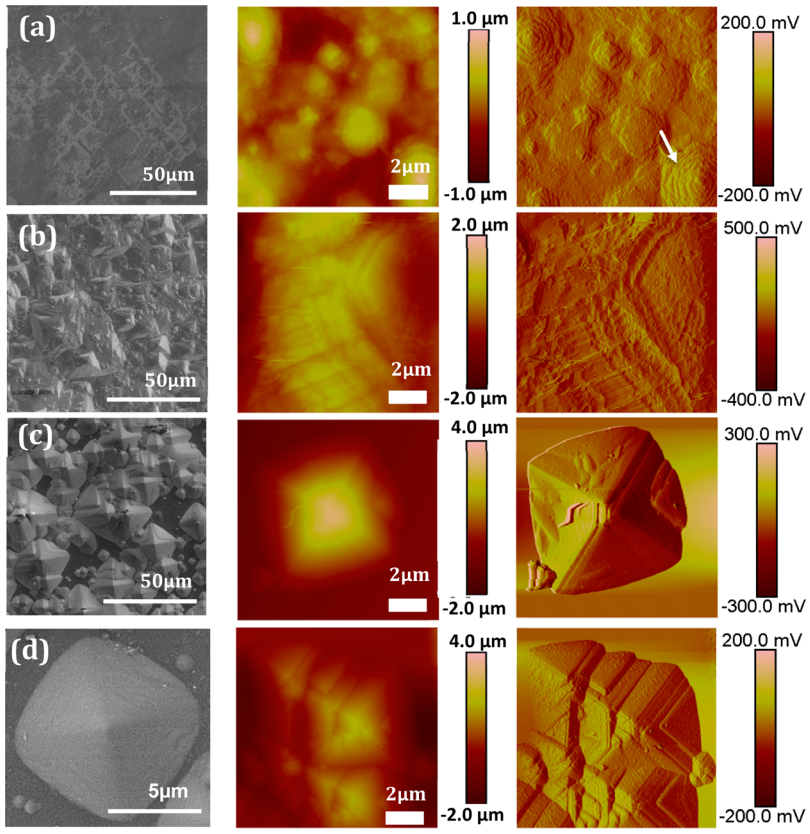

Figure 1. Growth of pyramidal arrays on Si(100) surfaces. SEM (left) and AFM height (center) and phase shift (right) images taken after (a) 0.5 h, (b) 1.0 h, (c) 2 h, and (d) two cycles of 2 h reactions (see also Figure 2c) at 100 °C. Arrow in (a) highlights the spiral pattern of the steps.

EtOH-washed Si(100) substrates were very smooth (see SI Figure S1a), but a 10 min reaction with the precursor mixture generated a surface roughness of about 10 nm (see SI Figure S1b). However, there were no detectable pyramidal structures at that point. After 20 min of reaction, silicate islands 200−500 nm in diameter and 120−170 nm in height were observed (see SI Figure S1c). Spiral patterns of steps characteristic of classical dislocation-controlled growth were observed after reaction times of 0.5−1 h. At this stage the pyramids exhibit a stepped structure with step heights of 45−60 nm (Figure 1a,b). These stepped pyramids grew from 3 to 4 μm to 4−6 μm in size during this half-hour period. Fully formed pyramids with a smooth surface were observed after 2.0 h of reaction (Figure 1c). Cooling the sample, introducing fresh precursor solution, and then repeating the reaction at 100 °C for another 2.0 h resulted in a higher packing density of identically shaped, coaligned, pyramidal structures (Figure 1d).

Deep UV Raman microprobe spectroscopy was employed to determine the chemical composition of the pyramidal particles. Measured Raman spectra have multiple bands between about 500 and 1100 cm^{-1} (Figure 2a), characteristic of silicate glasses and crystals.[28] The lower frequency mode at 500 cm^{-1} is associated with a bending vibration of the Si−O^- nonbridging oxygen group, and the higher frequency mode at 1100 cm^{-1} can be attributed to bond stretching vibration of the Si−O−Si bridging group. The results show that the pyramids consist of silicates; however, the small peak at 1426 cm^{-1} indicates CTAC incorporation in these pyramidal silicates (see also SI Figure S2). For pure silica[29] and crystalline silica polymorphs[30] no intense Raman bands are observed in the high-frequency region. Weaker Raman bands for silicates in the range 800 to 1200 cm^{-1} seen in the inset of Figure 2a are also critical to assignment of the symmetric Si−O stretch vibrations ν_s(Si−O^-) of a SiO_4 tetrahedron with 4, 3, 2, 1, and 0 bridging oxygens (Q_4, Q_3, Q_2, Q_1, and Q_0 species, around 1180, 1080, 1000, 920, and 850 cm^{-1}), resulting from the presence of network-modifying cations.[31] The Raman spectrum has a peak with stronger intensity at 1082 cm^{-1}, indicating that Q_3 species, as expected, are more abundant than the other species that may be present. Three other peaks at 1154, 1016, and 888 cm^{-1} can also be assigned to a relatively small amount of Q_4, Q_2, and Q_0 species. In addition, the shoulder at 971 cm^{-1} can also be assigned to a small amount of Q_1 species. Finally, a shift from 500 to 525 cm^{-1} is due to a distortion of bond angles on the Si(100) substrate.[32,33] Although there is no direct evidence for the formation of the complete stoichiometric $Na_2Si_2O_5$ layer on the Si(100) surface from XRD, likely due to the poor crystalline nature caused by the intimate mixture with the organic materials, the pyramidal silicate structures can be assigned as sodium disilicate ($Na_2Si_2O_5$) with CTAC incorporation based on these Raman spectra.[34]

Zero-temperature DFT and 100 °C *ab-initio* molecular dynamics simulations were used to investigate the interface between Si(100) and $Na_2Si_2O_5$ (Figure 2b). We investigated various polymorphs[35] of $Na_2Si_2O_5$ and concluded that the (001) surface of δ-$Na_2Si_2O_5$ matches most closely the Si(100) lattice. δ-$Na_2Si_2O_5$ has a monoclinic lattice with space group $P21/n$,[35] with a layered structure in the [001] direction. Therefore, the formation of a Si(100)/δ-$Na_2Si_2O_5$(001) interface is in line with layer-by-layer silicate growth observed

DOI: 10.1021/acsnano.6b03999
ACS Nano 2016, 10, 8670−8675

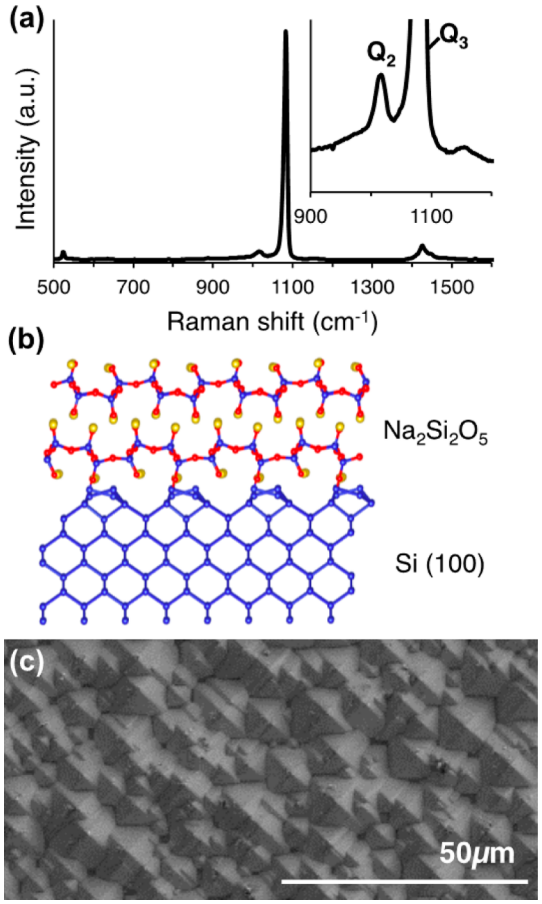

Figure 2. Structure of silicate on a Si(100) surface. (a) Raman spectrum of epitaxially grown pyramidal silicates on Si(100). (b) Simulated structure of $Na_2Si_2O_5$ on a Si(100) surface. Si atoms are shown as blue spheres, Na as yellow spheres, and O as red spheres. (c) Large-area SEM image of silicate taken after two cycles of 2 h reactions at 100 °C (see Figure 1d for the zoom-in image).

in AFM experiments. The results predict a stable epitaxial interface, based on long-time-scale dynamics with no decomposition or significant relaxation of the interface compared to that obtained in static energy minimization simulations. A lattice mismatch between Si(100) and sodium silicate of 9.6% is accommodated through the deformation of the interfacial layer of sodium silicate. This deformation is associated with rotation of SiO_4 tetrahedra to form bonds with surface Si atoms. The deformation is smaller for the next sodium silicate layer. Nevertheless this degree of lattice mismatch for inorganic solids is too high to support continuous film growth.[36] However, due to the flexibility of sodium silicate layers, such compressive strain can be accommodated during layer-by-layer growth of regular discrete particles,[37] such as the pyramidal particles observed in our SEM and AFM experiments. Such gradual relief of strain within the layered structure, which the simulations predict is achieved by each layer having different two-dimensional lattice vectors compared to their neighboring layers, suggests a loss of the overall bulk crystallinity in the [100] and [010] directions of sodium silicate, while the native lattice spacing in the [001] direction is less affected. This prediction is supported by X-ray diffraction (XRD) data, which do not show characteristic diffraction peaks between $2\theta = 15°$ and $2\theta = 40°$ for crystalline sodium silicate phases with different SiO_2/Na_2O molar ratios[38] (Figure S3). Instead, only a dominant diffraction peak at $2\theta = 69.16°$ and a very small diffraction peak at $2\theta = 32.96°$, characteristic of Si(004) and Si(002) from the silicon substrate,[39,40] were observed (see Figure S3). The incorporation of CTAC micelles into the silicate structure, as evidenced by the appearance of the characteristic CH_2 bending modes in Raman spectra at 1426 cm^{-1} (Figure 2a), is likely to provide an additional mechanism for strain relief within silicate layers. Surfactant incorporation also suggests that the silicate layers are not continuous even within a single pyramidal particle. Instead silicate layers are expected to form around the CTAC scaffold and have an array of extended defects.

Low-angle XRD indicates that, after reaction for 2 h at 100 °C, these pyramidal silicates have a cubic mesopore structure with $Pm\bar{3}n$ symmetry (Figure 3a), similar to that seen in previously reported mesoporous silicas.[41,42] Five well-resolved features indexed as (200), (210), (211), (320), and (400)

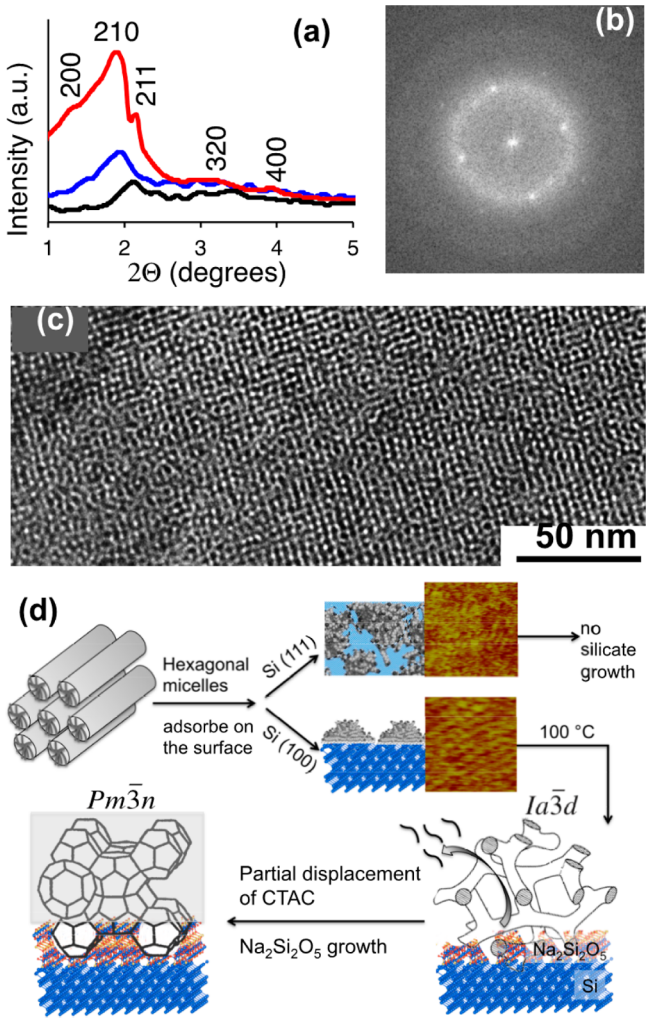

Figure 3. Structure and growth pathway of porous silicate pyramids on Si(100). (a) Low-angle XRD patterns of pyramidal silicates with cubic mesopores grown on a Si(100) surface at 100 °C for (1) 0.5 h, black line; (2) 1 h, blue line; and (3) 2 h, red line. (b) Electron diffraction pattern and (c) TEM image of cracked silicate with $Pm\bar{3}n$ pore symmetry along the [110] direction. (d) Schematic of surfactant-directed silicate formation process showing transformations in the surfactant template. More detailed AFM images of surfactant layers on Si(100) and Si(111) surfaces are given in the Supporting Information (Figures S4–S6).

DOI: 10.1021/acsnano.6b03999
ACS Nano 2016, 10, 8670–8675

reflections are also clearly observed. The cubic mesostructure was not clear during early stages of the process, but after reaction for over 1 h rapid transformation to a stable cubic structure was found.[43] The unit cell parameter of the $Pm\bar{3}n$ lattice, a, as calculated from the (210) diffraction peak, is 92 Å. This cubic micellar structure of the pyramidal silicates was further confirmed by the transmission electron microscopy (TEM), which revealed regular periodic pores over a large area (Figure 3). These findings clearly indicate that the pyramidal silicates exhibit a well-ordered mesoporous structure. The mesoscale structure can be calcined at above 500 °C to remove the surfactant without damaging the structural integrity to produce ordered mesoporous materials.

The mechanism for the growth of these organosilicates can be understood based on the details of CTAC self-assembly in solution and on Si surfaces combined with the epitaxial relationship of the Si(100)−sodium silicate interface. In the concentration range of 45−70 wt %, CTAC is known to form cylindrical micelles in aqueous solution at room temperature.[44] Our molecular simulations predicted that such cylindrical micelle geometry is retained upon micelle adsorption on the Si(100) surface.[45] Moreover, these micelles follow the topography of the Si substrate, resulting from the $c(4 \times 2)$ reconstruction of the (100) surface, and are arranged in a regular array with the long axis along Si[100] direction (Figure 3d). Such micelle morphology and orientation with respect to the protruding ridges on the reconstructed Si(100) surface maximizes the strength of the hydrophobic interactions between CTAC and the substrate.[45] AFM data confirm the formation of a highly oriented surfactant structure on the Si(100) surface (see Figure 3d and Figure S4). The 0.7 nm height and 6.5 nm spacing between the neighboring stripes in the AFM images are in-line with those previously observed for CTAB on graphite, an almost identical surfactant on a hydrophobic surface; this pattern was interpreted to be that of hemicylindrical structures.[46,47]

On the basis of these experimental data and theoretical predictions for the initial and final stages of templated growth of sodium silicate pyramids on Si(100), we propose the following pathway. The first stage of the reaction is likely to involve the transformation from a hexagonal micellar surfactant structure to a bicontinuous cubic structure (space group $Ia\bar{3}d$) upon heating to 100 °C. Although it is challenging to experimentally observe this temperature-induced phase transition on the Si surface, the transformation is expected based on the CTAC phase diagram.[44] This bicontinuous surfactant phase then provides a three-dimensional template for the growth of porous silicates. We note that, upon silicate growth, the surfactant may be partially displaced (schematically shown in Figure 3d). Such local reduction in surfactant volume fraction was reported to trigger transformation of the surfactant $Ia\bar{3}d$ phase to a micellar cubic $Pm\bar{3}n$ structure,[48] as observed in the final product.

In contrast to the situation on the Si(100) face, such a pathway for transformation of the surfactant template from hexagonal to bicontinuous cubic and to micellar cubic phase (Figure 3b) is not possible on a Si(111) surface. On this surface, surfactants do not retain their hexagonal micelle structure. Instead, as revealed by our AFM data (Figure 3d and Figure S4) and molecular dynamics simulations, surface symmetry dictates the formation of hemispherical CTAC micelles.[45] These micelles are randomly arranged on Si(111) and do not support the formation of a well-ordered three-dimensional template. As a result, no silicate growth is observed on this substrate under otherwise identical conditions (Figures S5 and S6).

Similarly, if the CTAC concentration is too low (*e.g.*, 100 mM) to support the transition to the bicontinuous phase at 100 °C, no ordered porous silicate is formed on Si(100). Instead, irregular mesoporous particles with poorly developed morphology are observed (Figure S7). In contrast, increasing the CTAC concentration while within the hexagonal phase stability region at room temperature produces more stable templates, hindering further transformation to the surfactant cubic phase. As a result, the increase in CTAC concentration to 150 mM produced dodecahedral shape silicate precipitates, but with slightly deformed cubic pore morphology (SI Figures S8 and S9). Elevation of temperature facilitates the transition from hexagonal to bicontinuous cubic phase at lower CTAC concentrations. For a CTAC concentration of 125 mM, 100−110 °C is an optimal temperature for producing well-defined organosilicate crystals. In these conditions the reaction of 20−30 mL of reaction mixture is completed in 2 h, and the repeat of the reaction produces homogeneous silicate pyramidal crystal arrays.

CONCLUSION

In conclusion, Si(100) surfaces can act as templates for growth of long-range-ordered, uniform crystal-like pyramidal silicates with cubic mesopores. Detailed characterization and modeling revealed that the Si(100) surface plays the dual role of a substrate for epitaxial growth of sodium silicate and one that directs CTAC self-assembly. The resulting highly ordered mesophase crystals and pore structure are a consequence of a series of transformations in surfactant template geometry from hexagonal phase to micellar cubic. Such complex nucleation and growth pathways to ordered three-dimensional architectures involving a series of transformations of organic templating agents are reminiscent of biomineralization processes. The latter often involves complex transformations in organic (protein) and inorganic phases ultimately leading to highly ordered hierarchical materials.[49] In this study we demonstrate the same level of control over materials architecture in a purely synthetic system. The mechanistic model of the synthesis pathway developed here broadens the horizons for knowledge-based design of ordered hierarchical materials for practical applications.

METHODS

Synthesis. In a typical synthesis of silicate pyramids on a Si(100) surface, 1,2-bis(trimethoxysilyl)ethane [$(CH_3O_3Si\text{-}CH_2CH_2\text{-}Si(OCH_3)_3)$] was added to a mixture of cetyltrimethylammonium chloride, sodium hydroxide, and water under vigorous stirring at room temperature, and this solution was aged for 24 h. The molar ratio of BTME:CTAC:NaOH:H_2O is 1.0:0.6−0.9:2.10:353. The aged solution was transferred to a Teflon container, and a small Si(100) piece was placed vertically into the solution. The Teflon container was placed in the oven at 100 °C for 2 h. The Si(100) piece was taken out of the container and washed with DI water.

Characterization. The XRD patterns were obtained on a Philips X'ert MPD X-ray diffractometer using Cu Kα (1.540 59 Å) radiation with the X-ray generator operating at 45 kV and 40 mA. TEM images were obtained on a JEOL JEM 2010 microscope. For TEM analysis, pyramidal silicates were carefully scratched from the Si surface. Raman spectra were excited using 244 nm cw radiation from a Lexel model 85SHG laser equipped with harmonic doubling optics. For Raman spectra measurement, approximately 10 mW of the filtered probe

DOI: 10.1021/acsnano.6b03999
ACS Nano 2016, 10, 8670−8675

radiation was directed into a confocal microscope stage (Olympus model U-5RE-2) having a 40× UVB objective. Backscattered light was collected, filtered to remove the excitation wavelength, and imaged through 100 μm slits into an 800 mm FL LabRAM HR spectrometer equipped with a 2400 g/mm grating blazed at 250 nm. A 5 s exposure time was used, multiple spectra were acquired for each sample, and the signal was averaged. All *ex-situ* AFM images were captured in tapping mode at room temperature (23 °C) with a NanoScope 8 atomic force microscope (Digital Instruments J scanner, Bruker) with silicon tips (model AC160TS-R3, rectangular lever, k = 26 N/m, tip radius 9 ± 2 nm; resonance frequency 300 kHz in air; Asylum Research). The drive amplitude was about 20 nm in air, and the signal-to-noise ratio was maintained above 10. The scanning speed was 1−2 Hz. The amplitude set-point was carefully tuned to minimize the average loading force (~50 pN) during imaging.

Simulations. The first-principles simulations were performed using the projector augmented wave method[50,51] implemented in VASP code.[52−54] The generalized gradient approximation parametrized by Perdew, Burke, and Ernzerhof was used for the exchange−correlation terms,[55,56] and wave functions were expanded by plane waves with a cutoff energy of 500 eV. The atomic positions were optimized until residual ionic forces became less than 0.02 eV Å^{-1}. A 2 × 2 × 1 Monkhorst−Pack grid was used. A 3 × 4 Si(100) supercell (120 atoms) and the corresponding 2 × 2 d-$Na_2Si_2O_5$ supercell (144 atoms) were used to construct the interface. A 25 Å vacuum gap was used in the direction normal to the interface.

Ab-initio molecular dynamics simulations at 373 K (100 °C) were performed within the canonical (NVT) ensemble. A Verlet algorithm was integrated with Newton's equations of motion at a time step of 2 fs for a total simulation time of 30 ps. The frequency of the temperature oscillations was controlled by the Nosé mass during the simulations. K-point sampling at the Γ-point was used.

ASSOCIATED CONTENT

Supporting Information

The Supporting Information is available free of charge on the ACS Publications website at DOI: 10.1021/acsnano.6b03999.

Additional AFM and TEM images of various stages of organosilicate growth on Si surfaces; Raman and XRD spectra of silicate particles (PDF)

AUTHOR INFORMATION

Corresponding Authors

*E-mail (M. L. Sushko): maria.sushko@pnnl.gov.
*E-mail (J. Liu): jun.liu@pnnl.gov.

Notes

The authors declare no competing financial interest.

ACKNOWLEDGMENTS

This work was supported by the Office of Basic Energy Sciences, Division of Materials Sciences and Engineering, U.S. Department of Energy, under Award KC020105-FWP12152. The TEM and SEM studies were conducted at the Environmental Molecular Sciences Laboratory, a national scientific user facility sponsored by the DOE's Office of Biological and Environmental Research and located at Pacific Northwest National Laboratory (PNNL). Simulations were performed using PNNL Institutional Computing resources. PNNL is a multiprogram national laboratory operated by Battelle for the DOE.

REFERENCES

(1) Wu, X. J.; Chen, J. Z.; Tan, C. L.; Zhu, Y. H.; Han, Y.; Zhang, H. Controlled Growth of High-Density CdS and CdSe Nanorod Arrays on Selective Facets of Two-Dimensional Semiconductor Nanoplates. *Nat. Chem.* **2016**, *8*, 470−475.

(2) Fan, Z. X.; Bosman, M.; Huang, X.; Huang, D.; Yu, Y.; Ong, K. P.; Akimov, Y. A.; Wu, L.; Li, B.; Wu, J.; Huang, Y.; Liu, Q.; Png, C. E.; Gan, C. L.; Yang, P. D.; Zhang, H. Stabilization of 4H Hexagonal Phase in Gold Nanoribbons. *Nat. Commun.* **2015**, *6*, 7684.

(3) Tan, C. L.; Zhang, H. Epitaxial Growth of Hetero-Nanostructures Based on Ultrathin Two-Dimensional Nanosheets. *J. Am. Chem. Soc.* **2015**, *137*, 12162−12174.

(4) Fan, Z. X.; Zhu, Y. H.; Huang, X.; Han, Y.; Wang, Q. X.; Liu, Q.; Huang, Y.; Gan, C. L.; Zhang, H. Synthesis of Ultrathin Face-Centered-Cubic Au@Pt and Au@Pd Core-Shell Nanoplates from Hexagonal-Close-Packed Au Square Sheets. *Angew. Chem., Int. Ed.* **2015**, *54*, 5672−5676.

(5) Tan, C. L.; Zeng, Z. Y.; Huang, X.; Rui, X. H.; Wu, X. J.; Li, B.; Luo, Z. M.; Chen, J. Z.; Chen, B.; Yan, Q. Y.; Zhang, H. Liquid-Phase Epitaxial Growth of Two-Dimensional Semiconductor Hetero-nanostructures. *Angew. Chem., Int. Ed.* **2015**, *54*, 1841−1845.

(6) Mazet, L.; Yang, S. M.; Kalinin, S. V.; Schamm-Chardon, S.; Dubourdieu, C. A Review Of Molecular Beam Epitaxy of Ferroelectric $BaTiO_3$ Films on Si, Ge and GaAs Substrates and Their Applications. *Sci. Technol. Adv. Mater.* **2015**, *16*, 036005.

(7) Li, G.; Wang, W.; Yang, W.; Wang, H. Epitaxial Growth of Group III-Nitride Films by Pulsed Laser Deposition and Their Use in the Development of LED Devices. *Surf. Sci. Rep.* **2015**, *70*, 380−423.

(8) Chambers, S. A. Molecular Beam Epitaxial Growth of Doped Oxide Semiconductors. *J. Phys.: Condens. Matter* **2008**, *20*, 264004.

(9) Monnier, A.; Schuth, F.; Huo, Q.; Kumar, D.; Margolese, D.; Maxwell, R. S.; Stucky, G. D.; Krishnamurty, M.; Petroff, P.; Firouzi, A.; Janicke, M.; Chmelka, B. F. Cooperative Formation of Inorganic-Organic Interfaces in the Synthesis of Silicate Mesostructures. *Science* **1993**, *261*, 1299−1303.

(10) Bagshaw, S. A.; Prouzet, E.; Pinnavaia, T. J. Templating of Mesoporous Molecular-Sieves by Nonionic Polyethylene Oxide Surfactants. *Science* **1995**, *269*, 1242−1244.

(11) Bao, X. Y.; Li, X.; Zhao, X. S. Synthesis of Large-Pore Methylene-Bridged Periodic Mesoporous Organosilicas and Its Implications. *J. Phys. Chem. B* **2006**, *110*, 2656−2661.

(12) Inagaki, S.; Guan, S.; Ohsuna, T.; Terasaki, O. An Ordered Mesoporous Organosilica Hybrid Material with a Crystal-Like Wall Structure. *Nature* **2002**, *416*, 304−307.

(13) Guan, S.; Inagaki, S.; Ohsuna, T.; Terasaki, O. Cubic Hybrid Organic-Inorganic Mesoporous Crystal with a Decaoctahedral Shape. *J. Am. Chem. Soc.* **2000**, *122*, 5660−5661.

(14) Inagaki, S.; Guan, S.; Fukushima, Y.; Ohsuna, T.; Terasaki, O. Novel Mesoporous Materials with a Uniform Distribution of Organic Groups and Inorganic Oxide in Their Frameworks. *J. Am. Chem. Soc.* **1999**, *121*, 9611−9614.

(15) Kim, J. M.; Kim, S. K.; Ryoo, R. Synthesis of MCM-48 Single Crystals. *Chem. Commun.* **1998**, 259−260.

(16) Xia, Y. D.; Mokaya, R. To Stir or Not to Stir: Formation of Hierarchical Superstructures of Molecularly Ordered Ethylene-Bridged Periodic Mesoporous Organosilicas. *J. Mater. Chem.* **2006**, *16*, 395−400.

(17) Wang, J. W.; Xia, Y. D.; Wang, W. X.; Poliakoff, M.; Mokaya, R. Synthesis of Mesoporous Silica Hollow Spheres in Supercritical CO_2/Water Systems. *J. Mater. Chem.* **2006**, *16*, 1751−1756.

(18) Yang, Z. X.; Xia, Y. D.; Mokaya, R. Periodic Mesoporous Organosilica Mesophases Are Versatile Precursors for the Direct Preparation of Mesoporous Silica/Carbon Composites, Carbon and Silicon Carbide Materials. *J. Mater. Chem.* **2006**, *16*, 3417−3425.

(19) Vercaemst, C.; de Jongh, P. E.; Meeldijk, J. D.; Goderis, B.; Verpoort, F.; Van Der Voort, P. Ethenylene-Bridged Periodic Mesoporous Organosilicas with Ultra-Large Mesopores. *Chem. Commun.* **2009**, 4052−4054.

(20) Morell, J.; Wolter, G.; Froba, M. Synthesis and Characterization of Highly Ordered Thiophene-Bridged Periodic Mesoporous Organo-silicas with Large Pores. *Chem. Mater.* **2005**, *17*, 804−808.

DOI: 10.1021/acsnano.6b03999
ACS Nano 2016, 10, 8670−8675

(21) Kapoor, M. P.; Yang, Q. H.; Inagaki, S. Self-Assembly of Biphenylene-Bridged Hybrid Mesoporous Solid with Molecular-Scale Periodicity in the Pore Walls. *J. Am. Chem. Soc.* **2002**, *124*, 15176−15177.
(22) Yang, Q. H.; Kapoor, M. P.; Inagaki, S. Sulfuric Acid-Functionalized Mesoporous Benzene-Silica with a Molecular-Scale Periodicity in the Walls. *J. Am. Chem. Soc.* **2002**, *124*, 9694−9695.
(23) Dunphy, D. R.; Garcia, F. L.; Kaehr, B.; Khripin, C. Y.; Collord, A. D.; Baca, H. K.; Tate, M. P.; Hillhouse, H. W.; Strzalka, J. W.; Jiang, Z.; Wang, J.; Brinker, C. J. Tricontinuous Cubic Nanostructure and Pore Size Patterning in Mesostructured Silica Films Templated with Glycerol Monooleate. *Chem. Mater.* **2011**, *23*, 2107−2112.
(24) Ciriminna, R.; Fidalgo, A.; Pandarus, V.; Beland, F.; Ilharco, L. M.; Pagliaro, M. The Sol-Gel Route to Advanced Silica-Based Materials and Recent Applications. *Chem. Rev.* **2013**, *113*, 6592−6620.
(25) Kruk, M. Access to Ultralarge-Pore Ordered Mesoporous Materials through Selection of Surfactant/Swelling-Agent Micellar Templates. *Acc. Chem. Res.* **2012**, *45*, 1678−1687.
(26) Mizoshita, N.; Tani, T.; Inagaki, S. Syntheses, Properties and Applications of Periodic Mesoporous Organosilicas Prepared from Bridged Organosilane Precursors. *Chem. Soc. Rev.* **2011**, *40*, 789−800.
(27) Lei, X. L.; Jee, Y.; Huang, K. Amorphous $Na_2Si_2O_5$ as a Fast Na^+ Conductor: an Ab Initio Molecular Dynamics Simulation. *J. Mater. Chem. A* **2015**, *3*, 19920−19927.
(28) Simon, I. *Modern Aspect of the Vitreous State*; Butterworths: London, 1960; Vol. *1*.
(29) Galeener, F. L.; Lucovsky, G. Longitudinal Optical Vibrations in Glasses - GeO_2 and SiO_2. *Phys. Rev. Lett.* **1976**, *37*, 1474−1478.
(30) Bates, J. B. Raman Spectra of Alpha-Cristobalite and Beta-Cristobalite. *J. Chem. Phys.* **1972**, *57*, 4042.
(31) Virgo, D.; Mysen, B. O.; Kushiro, I. Anionic Constitution of 1-atm Silicate Melts - Implications for the Structure of Igneous Melts. *Science* **1980**, *208*, 1371−1373.
(32) Furukawa, T.; Fox, K. E.; White, W. B. Raman-Spectroscopic Investigation of the Structure of Silicate-Glasses 0.3. Raman Intensities and Structural Units in Sodium-Silicate Glasses. *J. Chem. Phys.* **1981**, *75*, 3226−3237.
(33) Hass, M. Raman Spectra of Vitreous Silica, Gerrnania and Sodium Silicate Glasses. *J. Phys. Chem. Solids* **1970**, *31*, 415−422.
(34) You, J. L.; Jiang, G. C.; Xu, K. D. Temperature Dependence of the Raman Spectra of $Na_2Si_2O_5$. *Chin. Phys. Lett.* **2001**, *18*, 408−410.
(35) Kahlenberg, V.; Dorsam, G.; Wendschuh-Josties, M.; Fischer, R. X. The Crystal Structure of *delta*-$Na_2Si_2O_5$. *J. Solid State Chem.* **1999**, *146*, 380−386.
(36) Narayan, J.; Larson, B. C. Domain Epitaxy: A Unified Paradigm for Thin Film Growth. *J. Appl. Phys.* **2003**, *93*, 278−285.
(37) Fitzgerald, E. A. Gesi/Si Nanostructures. *Annu. Rev. Mater. Sci.* **1995**, *25*, 417−454.
(38) Woinaroschy, A.; Isopescu, R.; Filipescu, L. X-Ray Patterns Identification of Crystalized Sodium Disilicates Mixtures. *Cryst. Res. Technol.* **2000**, *35*, 969−977.
(39) Chen, Y.; Guo, L. P.; Chen, F.; Wang, E. G. Synthesis and Characterization of C_3N_4 Crystalline Films on Silicon. *J. Phys.: Condens. Matter* **1996**, *8*, L685−L690.
(40) Ozaki, K.; Hanatani, T.; Nakamura, T. Analysis of Crystalline Phases in Airborne Particulates by Grazing Incidence X-Ray Diffractometry. *Analyst* **2005**, *130*, 1059−1064.
(41) Huo, Q. S.; Margolese, D. I.; Ciesla, U.; Feng, P. Y.; Gier, T. E.; Sieger, P.; Leon, R.; Petroff, P. M.; Schuth, F.; Stucky, G. D. Generalized Synthesis of Periodic Surfactant Inorganic Composite-Materials. *Nature* **1994**, *368*, 317−321.
(42) Sakamoto, Y.; Kaneda, M.; Terasaki, O.; Zhao, D. Y.; Kim, J. M.; Stucky, G.; Shim, H. J.; Ryoo, R. Direct Imaging of the Pores and Cages of Three-Dimensional Mesoporous Materials. *Nature* **2000**, *408*, 449−453.
(43) Che, S. N.; Kamiya, S.; Terasaki, O.; Tatsumi, T. The Formation of Cubic Pm(3)over-barn Mesostructure by an Epitaxial Phase Transformation from Hexagonal P6mm Mesophase. *J. Am. Chem. Soc.* **2001**, *123*, 12089−12090.
(44) Chen, Z. F.; Greaves, T. L.; Fong, C.; Caruso, R. A.; Drummond, C. J. Lyotropic Liquid Crystalline Phase Behaviour in Amphiphile-Protic Ionic Liquid Systems. *Phys. Chem. Chem. Phys.* **2012**, *14*, 3825−3836.
(45) Darkins, R.; Sushko, M. L.; Liu, J.; Duffy, D. M. The Effect of Surface Topography on the Micellisation of Hexadecyltrimethylammonium Chloride at the Silicon-Aqueous Interface. *J. Phys.: Condens. Matter* **2015**, *27*, 054008.
(46) Manne, S.; Gaub, H. E. Molecular-Organization of Surfactants at Solid-Liquid Interfaces. *Science* **1995**, *270*, 1480−1482.
(47) Manne, S.; Cleveland, J. P.; Gaub, H. E.; Stucky, G. D.; Hansma, P. K. Direct Visualization of Surfactant Hemimicelles by Force Microscopy of the Electrical Double-Layer. *Langmuir* **1994**, *10*, 4409−4413.
(48) Faunce, C. A.; Paradies, H. H. Two New Colloidal Crystal Phases of Lipid a-Monophosphate: Order-to-Order Transition in Colloidal Crystals. *J. Chem. Phys.* **2009**, *131*, 244708.
(49) Meldrum, F. C.; Colfen, H. Controlling Mineral Morphologies and Structures in Biological and Synthetic Systems. *Chem. Rev.* **2008**, *108*, 4332−4432.
(50) Blochl, P. E. Projector Augmented-Wave Method. *Phys. Rev. B: Condens. Matter Mater. Phys.* **1994**, *50*, 17953−17979.
(51) Kresse, G.; Joubert, D. From Ultrasoft Pseudopotentials to the Projector Augmented-Wave Method. *Phys. Rev. B: Condens. Matter Mater. Phys.* **1999**, *59*, 1758−1775.
(52) Kresse, G.; Hafner, J. Ab-Initio Molecular-Dynamics for Open-Shell Transition-Metals. *Phys. Rev. B: Condens. Matter Mater. Phys.* **1993**, *48*, 13115−13118.
(53) Kresse, G.; Furthmuller, J. Efficiency of Ab-Initio Total Energy Calculations for Metals and Semiconductors Using a Plane-Wave Basis Set. *Comput. Mater. Sci.* **1996**, *6*, 15−50.
(54) Kresse, G.; Furthmuller, J. Efficient Iterative Schemes for Ab Initio Total-Energy Calculations Using a Plane-Wave Basis Set. *Phys. Rev. B: Condens. Matter Mater. Phys.* **1996**, *54*, 11169−11186.
(55) Perdew, J. P.; Burke, K.; Wang, Y. Generalized Gradient Approximation for the Exchange-Correlation Hole of a Many-Electron System. *Phys. Rev. B: Condens. Matter Mater. Phys.* **1996**, *54*, 16533−16539.
(56) Perdew, J. P.; Burke, K.; Ernzerhof, M. Generalized Gradient Approximation Made Simple. *Phys. Rev. Lett.* **1996**, *77*, 3865−3868.

DOI: 10.1021/acsnano.6b03999
ACS Nano 2016, 10, 8670−8675